AFRL-AFOSR-UK-TR-2022-0098

Advances in Metamaterials

Segev, Mordechai
TECHNION ISRAEL INSTITUTE OF TECHNOLOGY
TECHNION CITY
HAIFA, , 32000
ISR

08/19/2022
Final Technical Report

Air Force Research Laboratory
Air Force Office of Scientific Research
European Office of Aerospace Research and Development
Unit 4515 Box 14, APO AE 09421

REPORT DOCUMENTATION PAGE

PLEASE DO NOT RETURN YOUR FORM TO THE ABOVE ORGANIZATION.

1. REPORT DATE	2. REPORT TYPE	3. DATES COVERED	
20220819	Final	START DATE 20180518	END DATE 20220517

4. TITLE AND SUBTITLE
Advances in Metamaterials

5a. CONTRACT NUMBER	5b. GRANT NUMBER	5c. PROGRAM ELEMENT NUMBER
	FA9550-18-1-0208	
5d. PROJECT NUMBER	**5e. TASK NUMBER**	**5f. WORK UNIT NUMBER**

6. AUTHOR(S)
Mordechai Segev

7. PERFORMING ORGANIZATION NAME(S) AND ADDRESS(ES)
TECHNION ISRAEL INSTITUTE OF TECHNOLOGY
TECHNION CITY
HAIFA 32000
ISR

8. PERFORMING ORGANIZATION REPORT NUMBER

9. SPONSORING/MONITORING AGENCY NAME(S) AND ADDRESS(ES)	10. SPONSOR/MONITOR'S ACRONYM(S)	11. SPONSOR/MONITOR'S REPORT NUMBER(S)
EOARD UNIT 4515 APO AE 09421-4515	AFRL/AFOSR IOE	AFRL-AFOSR-UK-TR-2022-0098

12. DISTRIBUTION/AVAILABILITY STATEMENT
A Distribution Unlimited: PB Public Release

13. SUPPLEMENTARY NOTES

14. ABSTRACT
This project aims to explore new ideas related to Metamaterials and have a clear promise in defense-related applications, and bring them an important step forward towards implementation in the relevant industry. This final report reflects the Year 3 reports for all PI's, with an update for the results of Prof. Segev, Prof. Sebbah and Prof. Steinberg for the period of June, 2021 – May, 2022. Professors Sebbah and Steinberg are those who requested the one-year no-cost extension (which is why it was important to have their updated report), and Professor Segev decided to update his
report following several major discoveries made by his group, which resulted in papers in Nature and Science.

15. SUBJECT TERMS

16. SECURITY CLASSIFICATION OF:			17. LIMITATION OF ABSTRACT	18. NUMBER OF PAGES
a. REPORT U	b. ABSTRACT U	c. THIS PAGE U	SAR	18

19a. NAME OF RESPONSIBLE PERSON	19b. PHONE NUMBER *(Include area code)*
ATTILA SZEP	314 235 6044

Advances in Metamaterials

PI: Distinguished Prof. Mordechai (Moti) Segev
msegev@tx.technion.ac.il
Technion – Israel Institute of Technology, Israel
Dept. of Physics, Technion City Campus, Haifa 3200003 Israel
+972-4-829-3926
+972-4-822-1514

Co-PIs:
Prof. Erez Hasman
mehasman@technion.ac.il
Technion – Israel Institute of Technology, Haifa
Dept. of Mechanical Engineering, Technion City, Campus, Haifa 3200003 ISRAEL
+972-77-887-2916
+972-77-8875711

Prof. Yonina C. Eldar
yonina.eldar@weizmann.ac.il
Weizmann institute of Science, Rehovot
Dept. of Mathematics and Computer Science, Weizmann institute of Science, Rehovot 7610001, Israel.
+972-8-9343702
+972-8-9343218

Prof. Uriel Levy
ulevy@mail.huji.ac.il
The Hebrew University Of Jerusalem, Israel.
Dept. of Applied Physics, Hebrew University of Jerusalem, Israel
+972-2-65-84256

Prof. Ben Z. Steinberg
steinbrg@tauex.tau.ac.il
Tel Aviv University, Israel.
Electrical Engineering Dept., Tel Aviv University, Israel
+972-3-6407373
+972-3-6423508

Prof. Patrick Sebbah
patrick.sebbah@biu.ac.il
Bar Ilan University, Israel
Dept. of Physics, Bar Ilan University, Israel
+972-3-5314420
+972-3-5314105

Final Report for May 18, 2018 – May 17, 2022 (No-cost extension – Year 4)

Abstract:

This project aims to explore new ideas related to Metamaterials and have a clear promise in defense-related applications, and bring them an important step forward towards implementation in the relevant industry.

This final report reflects the Year 3 reports for all PI's, with an update for the results of Prof. Segev, Prof. Sebbah and Prof. Steinberg for the period of June, 2021 – May, 2022. Professors Sebbah and Steinberg are those who requested the one-year no-cost extension (which is why it was important to have their updated report), and Professor Segev decided to update his report following several major discoveries made by his group, which resulted in papers in Nature and Science.

Overall, this project has six groups working on separate tasks.

Below we briefly describe the main research results for each of the six teams, as obtained in the final year of the project.

I. Topological Insulator Laser / M. Segev

During the past 2 years, we worked on several ideas related to this project. In what follows, I will describe one major result, which has been accepted to **Nature magazine** and will be appearing in 2 weeks [1]. It describes the first experimental realization of a three-dimensional photonic topological insulator. This is also the first 3D topological insulator induced by a dislocation – in any system ever studied.

In addition, we also used the AFOSR funding to seed a new project on Photonic Time-Crystals, and published a few papers on this new topic [2-4]. The most important one is about amplified emission and lasing in Photonic Time-Crystals, which appeared in Science magazine two months ago [2]. This new concept is described in great details in a new proposal submitted to AFOSR.

Three-Dimensional Photonic Topological Insulator

The hallmark of topological insulators is the scatter-free propagation of waves in topologically protected edge channels. This transport is strictly unidirectional on the outer edge of the medium, and therefore capable of bypassing sharp corners and imperfections, even in the presence of substantial disorder. In photonics, two-dimensional topological edge-states have been demonstrated on several different platforms, and are emerging as a promising tool for robust lasers, quantum emitters, optical isolators and other applications. *In a recent breakthrough which will be submitted in a week or so to a major journal, we demonstrated a three-dimensional photonic topological insulator induced by a screw dislocation.* For this purpose, we utilized the concept of synthetic dimensions on in a 2D photonic waveguide array by introducing an additional modal dimension to transform the system into a 3D photonic topological insulator. The lattice dislocation endows the system with edge states propagating on three-dimensional trajectories, with protection akin to strong photonic topological insulators.

Three-dimensional topological insulators are generally divided into two categories: weak and strong. Strong topological insulators host 3D edge states on all of their surfaces, and are impervious to variations in the shape of the crystal or variation that are small compared to the bandgap energy. In contrast, weak 3D topological insulators topologically are equivalent to stacked arrangements of 2D topological insulators to form a 3D crystal. For example, a 3D cubic lattice with a constant magnetic field along one of the lattice axes is known to form a 3D weak topological insulator (Fig.1A). Since each of the 2D layers supports an edge state, the 3D composite structure is characterized by multiple edge states propagating on four surfaces in a 2D course (Fig.1B).

We implement the 3D topological insulator with a dislocation by employing lattices of helical optical waveguides with two spatial dimensions and one modal dimension, where the longitudinal spatial coordinate plays the role of time. To show how the light is propagating in a topologically protected fashion in all 3D – the two spatial dimensions and the synthetic modal one dimension, we study the propagation of the edge state in the 2D layers with three excitations (one in each mode) in the unperturbed region of the lattice (Fig. 2A-C). Since the modes are tightly localized, the position in modal space can be chosen by injecting light into one of the three waveguides. Far away from the dislocation, we indeed observe that the initial excitations remain in their initial modes as they propagate along the edge and around a corner, as shown in the intensity pictures at the output facet of the waveguide array (Fig.2D-F). For example, in Fig.2B we excite a wavepacket

on the edge that is entirely in the first mode, by exciting only the lowest waveguide in 4 columns along the upper edge. Since the modes are localized, we can directly identify the mode from observing the output intensity in the corresponding Fig.2E. Accordingly, the light at the output does not couple to other modes (stays at the lower waveguide of each column) and continue to propagate along the edge (green dashed box), bypassing the corner.

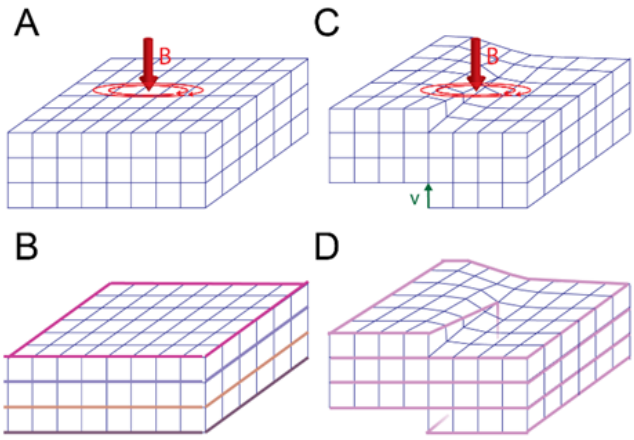

Figure 1: A weak topological insulator (TI) vs a weak TI with a dislocation. (A) An Illustration of a cubic lattice with a constant magnetic field along one of its axes, that maps to stacking layers of 2D TIs. (B) Edge states from the different square TIs that can couple to each other and form a gap. (C) A weak TI (from (A)) with a dislocation defined by the Burgers vector v. (D) In the presence of a screw dislocation, all individual edge state in a Weak TI merge into edge states that wind around the entire 3D system. These edge states do not map to degenerate edge states of a weak TI anymore, but instead give rise to a strong 3D topological insulator.

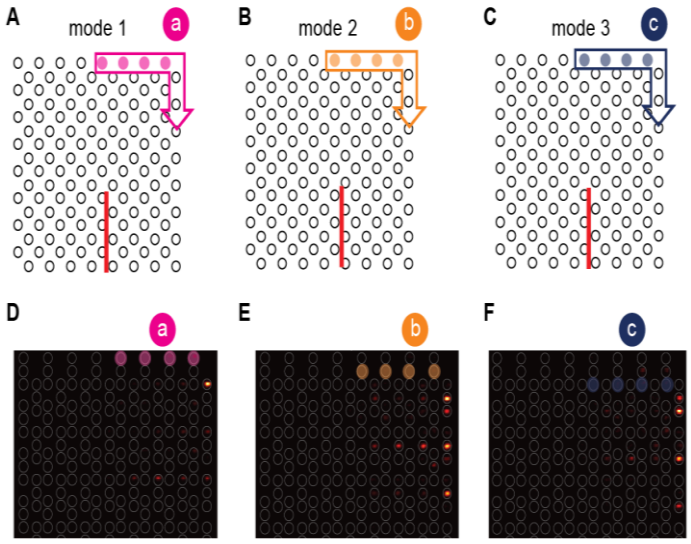

Fig. 2: **Experimentally viewed evolution of edge wavepackets in the of 3D synthetic-space topological insulator.** (A-C) Sketches showing the excitation in modal space of modes 1-3 respectively. The full circles are the excited waveguides in each of the modes, and the arrow points to the expected propagation direction in the topological phase. (D-F) Intensity images at the output facet of the structure. The painted circles mark the areas into which light is injected at the input. The light propagates away from the excitation region, passes the corner, and continues along the next (vertical) edge. At the output facet, the light is localized in each column in one of the 3 waveguides, where the lowest waveguide of the column represents mode 1, and the uppermost waveguide is mode 3. The mode is determined according to the position of the light in the column.

It is instructive to view the propagation in modal space near the dislocation (Fig. 3), where we excite the light near the dislocation, to observe the evolution in the modal dimension. Unlike the excitation presented in Fig.2, here, light injected into a certain mode and descends to the mode below it upon passing the dislocation ((b) and (c) in Fig.3A-C). The exception is when the light is injected into the first mode and has no mode to descend to ((a) in Fig.3A), the dislocation behaves as a barrier and the light flows around the dislocation without scattering, staying in the lowest mode. As in Fig.2A-C, Fig.3A-C shows the excitations and the evolution in 3D space, but unlike in Fig.3A-C, here the dislocation serves to transfer the light between different modes. We track each excitation with the colored letters (a-c).

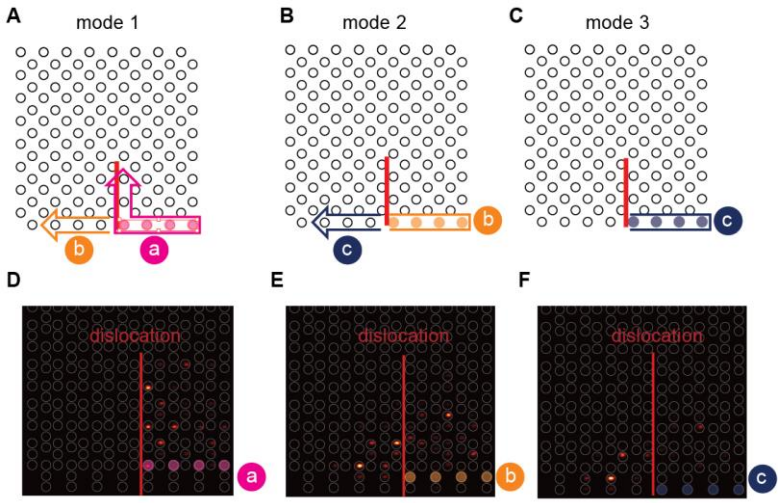

Fig. 3: **Experimentally viewed edge wavepackets bring transformed from each mode to the mode below it by the dislocation.** The markings are similar to Fig.3, but here the excitations are near the dislocation. (A-C) Sketches of the mode transfer driven by the dislocation. The full circles mark the excited sites and the arrow points to the propagation direction in the topological phase. (D-F) Intensity images at the output facet of our waveguide array. As in Fig.2, The colored centers mark the sites into which light is injected at the input. The mode is determined by the position of the light in the column. A colored letter (a-c) is attributed to each excitation.

Altogether, in this work we experimentally investigated the dynamics of edge states in a weak 3D photonic topological insulator, and showed hat the introduction of a screw dislocation endows the system with properties of a strong 3D topological insulator. This is the first observation of a 3D photonic topological insulator, and also the first 3D topological insulator in synthetic space in any system. We expect that this work will open the door for exploring topological phases in laboratory experiments in dimensions four and higher.

Publications

1. E. Lustig, L. Maczewsky, J. Beck, T. Biesenthal, M. Heinrich, Z. Yang, Y. Plotnik, A, Szameit and M. Segev, Photonic topological insulator induced by a dislocation in three dimensions, to appear, **Nature**, 2022.

2. T. M. Lyubarov, Y. Lumer, A. Dikopoltsev, Y, Sharabi and M. Segev, *Amplified emission and lasing in photonic time-crystals*, **Science** 377, 425-428 (2022).

3. A. Dikopoltsev, Y, Sharabi. M. Lyubarov, Y. Lumer, S. Tsesses, E. Lustig, I. Kaminer and M. Segev, *Light emission by free electrons in photonic time-crystals*, **Proc. Nat. Aca. Sci. (PNAS)** 119, e2119705119 (2022).

4. Y, Sharabi, A. Dikopoltsev, E. Lustig and M. Segev, *Spatiotemporal photonic crystals*, **Optica** 9, 585-592 (2022).

II. Multifunctional dielectric metasurface for coding and sensing of light / E. Hasman

Toward Atomic-Scale Spin-optics with Valley Excitons

Spin-optics is a valuable tool to investigate spin-dependent effects from integrated quantum emitters. The incorporation of an atomic-thin WSe_2 monolayer into a photonic crystal slab with geometric phase defects enables a valley information separation at room temperature, pushing the spin-optics toward an atomic scale.

Akin to electrons, photons possess an intrinsic angular momentum known as spin. By leveraging this spin degree of freedom, spin-optics has shown great potential for fundamental science and advanced applications.[1,2] In the pursuit of new spin-optical devices possessing large information capacity and high processing speed, a long-thought goal is to interface spin-optics and spintronics for an interchange of spin information between photons and electrons. This requires the miniaturization of spin-optical devices down to nanometric scales and beyond.

Currently, a family of atomic-thin materials has triggered intense research due to exotic electrical, optical, and thermal properties. In particular, direct bandgap transition metal dichalcogenide monolayers show opposite electronic spins at ±K valleys. Consequently, the valley information can be selectively encoded and retrieved by the photonic spin according to the valley-dependent optical selection rules. Although great efforts have been devoted into this field, previous strategies using metallic structures inherited intrinsic losses and limited functionalities. Alternatively, versatile geometric phase metasurfaces (GPMs) represent an attractive candidate to perform such a task. The GPMs are constructed to generate spin-dependent geometric phases that enable spin-controlled manipulations of light.[1] However, conventional GPMs are generally designed for plane waves, preventing an efficient interaction between nanoantennas and integrated valley excitons behaving as in-plane circular dipole emitters. Recently, we tackled this challenge by exploiting a novel platform of geometric phase defective photonic crystals (GP-PhCs).[3,4]

The GP-PhCs are composed of a PhC slab with isotropic nanopillars and a GPM with space-variant anisotropic nanoantennas that serve as defects. By utilizing bandgap of the PhC, the insertion of the GPM into the PhC slab gives rise to a near-field geometric phase defect mode, which couples the defects for an effective interaction with the integrated valley excitons, resulting in site-controlled excitation, photoluminescence enhancement, and spin-dependent manipulation of individual valley excitons. Consequently, a spin-split dispersion from valley excitons is observed in momentum space, manifesting as the photonic Rashba effect. Particularly, the spin-up/-down branches correspond to emission from ±K valley excitons, respectively, indicating a valley separation in momentum space at room temperature. Moreover, this basic interaction mechanism between circular dipole emitters and nanostructures can be generalized to quantum emitters with arbitrary in-plane polarizations and PhC structures with distinct symmetries.

We envision our all-dielectric GP-PhCs as a versatile platform for integrated spin manipulation, which establishes a multifunctional interface between valleytronics and photonics down to an atomic scale.

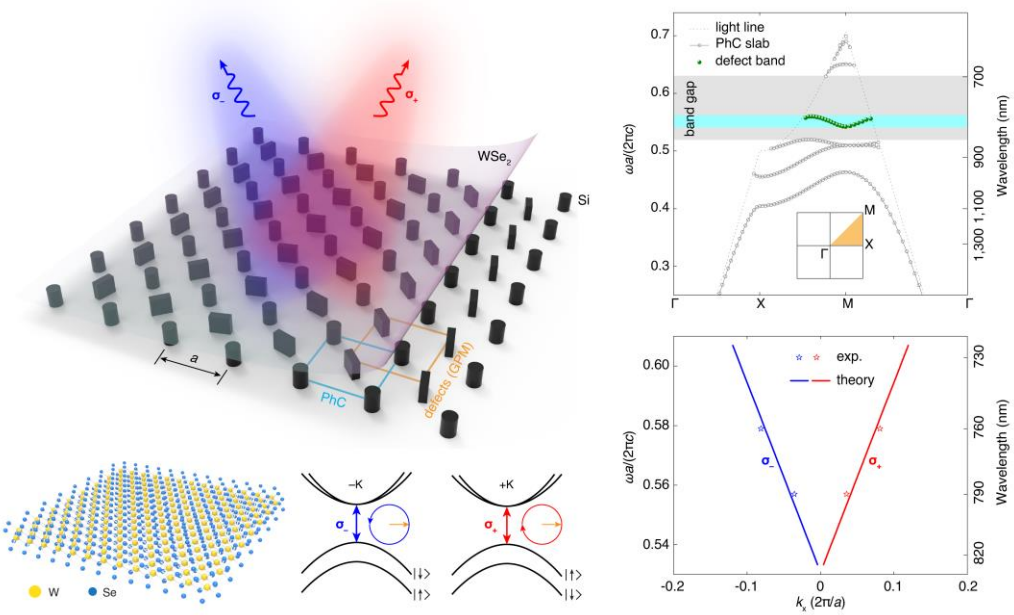

Fig 4. Upper left: Illustration of a GP-PhC/WSe_2 monolayer heterostructure. Lower left: Schematics of valley-dependent optical selection rules for ±K valley excitons. Upper right: Simulated defect band of a GP-PhC. Lower right: Measured spin-split dispersion from valley excitons.

[1] Z. Bomzon et al. Opt. Lett. 27, 1141 (2002).
[2] B. Wang et al. Nat. Nanotechnol. 15, 450 (2020).
[3] K. Rong et al. Nat. Nanotechnol. 15, 927 (2020).
[4] A. Krasnok, Nat. Nanotechnol. 15, 893 (2020).

A Spinning Glimpse of Nanoscale Fluctuations

An optical metrology that can detect extremely weak disorders in a deep-subwavelength resolution is critical for nanotechnology. However, disordered light—matter interactions are very subtle. The disorder and stochastic nature hinders light from detecting any useful information other than that from a homogeneous medium. In our work this year [1], we approached this challenge by exploiting light interaction with magnetized disorder metasurfaces. Nanoscale size fluctuations was revealed by the probability distribution of a stochastic photonic spin Hall effect (PSHE), which was induced by disordered magneto-optical Kerr rotations.

Magnetic fields can break the photonic spin symmetry—spin being the helicity of electromagnetic field. Metasurfaces are two-dimensional arrays of nanoantennas assembled in subwavelength periods. In our work, the metasurfaces are consisted of circular nickel nanoantennas with their radii randomly fluctuated in several nanometers. The random variations in the sizes of nanoantennas give rise to disordered geometric phases from magneto-optical Kerr rotations. This leads to a spin-dependent beam shift several orders of magnitude smaller than the diffraction limit of light, i.e., a PSHE [2, 3].

The experimental observation of the PSHE via a weak measurement [1-4] can be achieved by applying a pre-selection polarization and a nearly-orthogonal post-selection polarization. By evaluating the PSHEs from a large number of disordered metasurfaces with different randomizations, we observe a Gaussian probability distribution for the spin shifts. Notably, the

standard deviation of the Gaussian distribution is proportional to the size fluctuation of the nanoantennas. This result enabled us to detect a five-nanometer size fluctuation of nanoantennas.

Our novel approach can be extended for different types of geometric disorders and is potentially applicable for identifying nanometric non-uniformity in electronic and photonic chips. It also opens the avenue to measure small disorders in magnetic fields and magnetism, as well as investigate fluctuation phenomena in quantum mechanics.

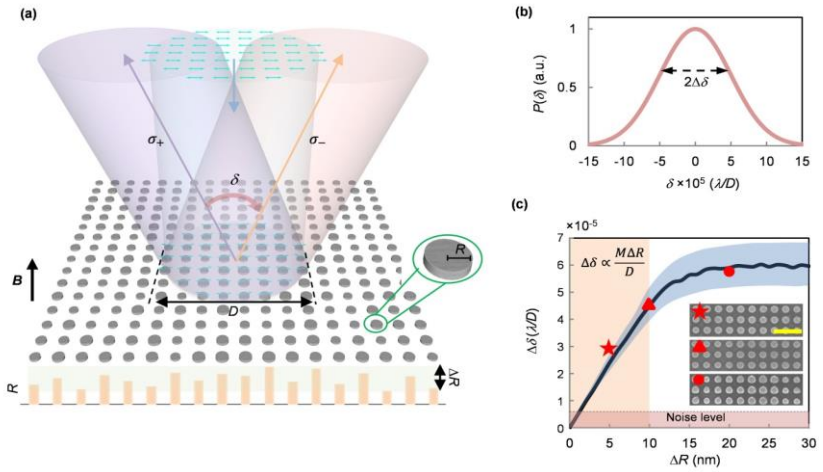

Fig 5. (a), The sketched PSHE from a magnetized disorder metasurface. A polarized incident beam (polarizations indicated by the cyan arrows) is reflected and split into spin up (σ+) and spin down (σ–) components with a subdiffraction-limited angle δ, due to disordered magneto-optical Kerr rotations (the disordered cyan arrows). R indicates the radius of a circular nanoantenna. D is the beam's diameter, and B is the magnetic field. The bottom panel exemplifies a radius distribution of disordered nanoantennas, with ΔR being the fluctuation. (b), The probability distribution of stochastic PSHEs $P(\delta)$, with $\Delta\delta$ being the standard deviation of the Gaussian distribution. λ is the wavelength of light. (c), Experimental and calculated $\Delta\delta$ vs. the radius fluctuation ΔR. M is magnetization. Insets: scanning electron microscopy images. Scale bar, 1 μm.

[1] B. Wang et al., Nat. Nanotech. 15, 450–456 (2020)
[2] B. Wang, et al., Phys. Rev. Lett. 123, 266101 (2019)
[3] E. Maguid, et al., Science 358, 1411 (2017)
[4] Y. Aharonov, D. Z. Albert, & L. Vaidman, Phys. Rev. Lett. 60, 1351–1354 (1988)

Publications

[1] K. Rong, B. Wang, A. Reuven, E. Maguid, B. Cohn, V. Kleiner, S. Katznelson, E. Koren, E. Hasman, *Photonic Rashba effect from quantum emitters mediated by a Berry-phase defective photonic crystal*, **Nature Nanotechnology** 15, 927 (2020)
[2] B. Wang, E Maguid, K Rong, M Yannai, V Kleiner and E Hasman, *Photonic topological spin Hall effect mediated by vortex pairs*, **Phys. Rev. Lett.** 123, 266101 (2019)

III . Advanced signal processing for metamaterials-based radar / Y.C. Eldar

Over the course of the last year, we have been working on two projects under the support of the AFOSR grant:

Near-field Wireless Communications with Dynamic Metasurface Antennas

Our main project considers the application of Metasurface antennas for near-field wireless communications. Dynamic Metasurface Antenna (DMA) is an emerging technology to realize large-scale planar antenna arrays with reduced cost and power consumption. When large arrays at high frequencies, such as DMA, are employed, wireless communications and wireless power transfer might take place in the radiating near-field (Fresnel) region where spherical wave propagation holds, rather than plane wave propagation as in the far-field. In radiating near-field, transmitters can generate focused beams, which can focus signal energy on specific locations rather than in a direction as conventional far-field beam steering, thus facilitating wireless communications and wireless power transfer systems.

In our work [1], submitted to the IEEE Transactions on Wireless Communications, we study the potential of near-field beam focusing for multi-user MIMO communication systems, where the base station is equipped with a DMA. We present a mathematical model for DMA-based near-field MIMO communications. We then characterize the sum-rate maximization problem of the considered system and propose an efficient solution to jointly design the DMA weights and digital precoding vector such that the achievable sum-rate is maximized. Our numerical results demonstrate that our design generates focused beams such that users residing at the same angular direction can communicate reliably without interfering, which is not achievable using conventional far-field beam steering. The focused beams in radiating near-field can also facilitate efficient wireless power transfer, and such capability is envisioned and presented in our article [2], which was submitted to the IEEE Communications Magazine. Following up [2], we study the exploitation of DMA to achieve such an energy focusing ability in multi-user WPT systems, detailed in the paper [3], where we demonstrated that using DMAs for energy focusing results in improved energy transfer efficiency in the radiating near-field with minimal energy pollution.

Dual Function Radar Communication Systems using Index Modulation

Our second project focuses on communication scheme integrated into radar systems. In a multitude of practical applications, such as autonomous vehicles, the communicating device must also be able to sense its environment using radar. Dual-function radar communication (DFRC) systems implement both sensing and communication using the same hardware, reducing the number of antennas, system size, weight, and power consumption, while allowing spectrum and resource sharing. In this project, we study the embedding of digital communication methods into radar systems (index modulation, IM) such that both functionalities can operate reliably with minimal mutual interference.

In our work [4], submitted to the IEEE Transactions on Signal Processing, we extend IM-based DFRC systems to utilize sparse arrays and frequency modulated continuous waveforms (FMCWs), which are popular in automotive radar for their simplicity and low hardware complexity. The proposed FMCW-based radar-communications system (FRaC) operates at reduced cost and complexity by transmitting with a reduced number of radio frequency modules, combined with

narrowband FMCW signalling. Our numerical results show that our proposed radar scheme achieves similar resolution performance compared with a wideband radar system operating with a large receive aperture, while requiring less hardware overhead. In [5], we design bit constrained communication receivers in dual-function systems, by considering hybrid analog/digital architectures and treating their operation as task-based quantization. Our simulation results demonstrate that the proposed task-based quantization strategy outperforms receivers operating only in the digital domain with the same total number of quantization bits. Moreover, a random pulse phase coding approach is proposed to resolve the range ambiguity of pulse-Doppler radars, which is detailed in the work [6], recently published at the IEEE Transactions on Signal Processing. Finally, the hardware prototypes built in our lab over the last year are detailed in the papers [7-8].

Publications

All the following references acknowledge the AFOSR support:

[1] H. Zhang, N. Shlezinger, F. Guidi, D. Dardari, M.F. Imani, Y. C. Eldar, "Beam Focusing for Near-Field Multi-User MIMO Communications", Submitted to the IEEE Transactions on Wireless Communications, 2021.

[2] H. Zhang, N. Shlezinger, F. Guidi, D. Dardari, M.F. Imani, Y. C. Eldar, "Near-field Wireless Power Transfer for 6G Internet-of-Everything Mobile Networks: Opportunities and Challenges", Submitted to the IEEE Communications Magazine, 2021.

[3] H. Zhang, N. Shlezinger, F. Guidi, D. Dardari, M.F. Imani, Y. C. Eldar, "Near-Field Wireless Power Transfer with Dynamic Metasurface Antennas", Submitted to the IEEE International Conference on Acoustics, Speech, and Signal Processing (ICASSP), 2021.

[4] D. Ma, N. Shlezinger, T. Huang, Y. Liu, and Y. C. Eldar, "FRaC: FMCW-Based Joint Radar-Communications System via Index Modulation", Submitted to IEEE Transactions on Signal Processing, June 2021.

[5] D. Ma, N. Shlezinger, T. Huang, Y. Liu, and Y. C. Eldar, "Bit Constrained Communication Receivers in Joint Radar Communications Systems", IEEE International Conference on Acoustics, Speech, and Signal Processing (ICASSP), Toronto, Canada, May 2021.

[6] X. Liu, D. Cohen, T. Huang, Y. Liu, and Y. C. Eldar, "Unambiguous Delay-Doppler Recovery from Random Phase Coded Pulses", IEEE Transactions on Signal Processing, vol. 69, pp. 4991-5004, August 2021.

[7] D. Ma, N. Shlezinger, T. Huang, Y. Shavit, M. Namer, Y. Liu, and Y. C. Eldar, "Spatial modulation for joint radar-communications systems: Design, analysis, and hardware prototype", IEEE Transactions on Vehicular Technology, vol. 70, no. 3, pp. 2283 - 2298, March 2021.

[8] R. Fu, S. Mulleti, T. Huang, Y. Liu, and Y. C. Eldar, "Hardware prototype demonstration of a cognitive radar with sparse array antennas", Electronics Letters, vol. 56, no. 22, pp. 1210-1212, Oct. 2020.

IV. High-index multilayer metasurfaces for broadband polarization control / U. Levy

(Collaboration with the group of A, Grbic, University of Michigan)

Two-dimensional transition metal dichalcogenides (TMDCs) are promising to become an important component in modern optoelectronic applications. The direct band gap in the monolayer TMDCs, shows interesting optical phenomena such as strong spin-valley coupling and valley coherence [1]. Recently, novel integration methods of TMDCs into photonic and plasmonic platforms have demonstrated a wide range of applications, like photo detectors and 2D nano lasers [2]. All the photonic crystal cavities integrated with 2D material platforms so far have sizes in the order of the wavelength. This reduces the quality of performance in the sub-wavelength regime due to field confinement breakdown at these length scales. In this context, it is important to develop new integration methods of TMDCs to photonic-plasmonic components with ultra-small mode volume and enhance light-matter interactions in the deep sub-wavelength limit. Hyperbolic metamaterials (HMM) are indefinite media which have hyperbolic dispersion in momentum space, contrary to the ellipsoidal or spherical dispersion of natural materials [3]. It has been shown recently that cavities made of these hyperbolic metamaterials show anomalous dispersion [4], and enhanced light-matter interaction at visible frequencies [5]. To enable the enhancement of solid-state light-emitting devices with 2D TMDC materials, we have designed and fabricated circular nano-scale HMM cavities (~100 nm × 125 nm) made up of alternating metallic and dielectric layers of 16 nm Ag and 24 nm Al2O3, respectively. The Q-factors of our HMM cavities are in the order of ~20 - 25, which is reasonable for metallic lossy cavities, but still very low compared to purely dielectric cavities. A useful figure of merit for light-matter interactions around nanocavities is *Q/Vm*, with *Vm* being the mode volume. For our case, $Vm \sim 5 \times 10^{-3}\lambda^3$, which results in *Q/Vm* values of ca. 5×10^5, which is a very high value for enhanced light-matter interactions using 2D TMDC materials.

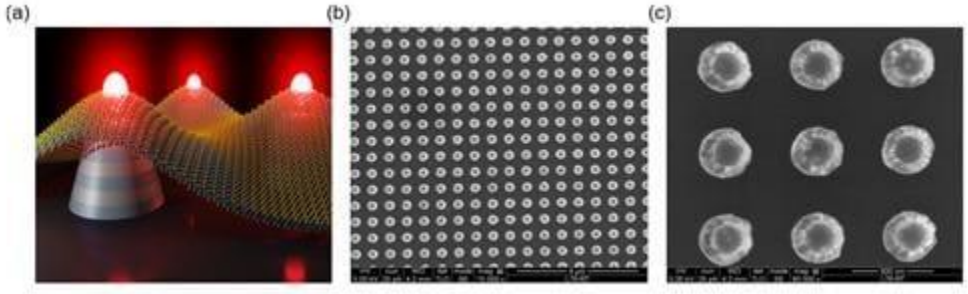

Fig.**6.a)** Schematic of the HMM cavity with 2D monolayer *WS2*. **b)** FESEM image of 110 nm radius HMM cavity and c) High FESEM image of 3 x 3 cavity array.

Figure 6 (a) shows the schematic diagram of the proposed experimental configuration, where single layer WS2 is covering the HMM cavities. The cavities were designed to have a resonance coupled to the emission spectrum of the TMDC layers. This allows us to demonstrate far-field emission enhancement, for potential applications in 2D TMDC quantum light emitting devices. We also tuned the spectral position of the cavity resonances by changing the lateral geometry of the cavities along different iso-frequency surfaces (hyperbolic dispersion relation). Figure 6 (b) and (c) shows the FESEM image of the fabricated HMM cavity array with different magnifications.

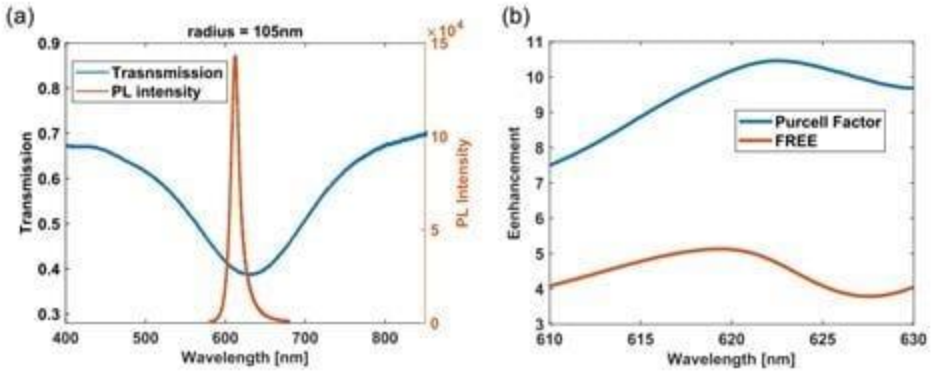

Fig.**7.a)** Experimental transmission measurement on 150 nm cavity showing cavity resonance over-lap with the experimental measured PL emission from the 2D monolayer of WS_2. **b)** Simulation of Purcell factor and FREE for in-plane dipole polarisation of excitons in 2D WS_2 monolayer placed on the HMM cavity.

Figure 7 (a) Shows the experimentally measured transmission spectrum of HMM cavities with a radius of 105 nm, and photoluminescence (PL) from the WS2 monolayer. From the figure it is clear that the cavity resonance overlaps with the emission spectrum of the 2D TMDC layer. Figure 7 (b) shows the numerical simulations of the Purcell factor of in-plane exciton dipoles of 2D TMDC WS2 placed on top of the HMM cavity. For all the cavity sizes the PL emission is enhanced compared to the TMDC monolayer emission on the glass substrate. By careful design of hyperbolic nano-scale cavities we have shown the large enhancement of the far field radiation up to ~ 10 fold in the WS2 emission frequency. Figure 7(b) also shows far-field emission enhancement (FREE) which indicates the radiative rate enhancement due to HMM cavities on 2D TMDC layers. The FREE is enhanced up to ~ 5 fold due to HMM cavities compared to the 2D materials on glass. These ultra-small mode volumes, with large Purcell factor, can be used for deep sub-wavelength low power nonlinear and quantum optics with 2D TMDC materials. In conclusion we have shown numerically enhancement of Purcell factor and far-field radiation of 2D TMDCs coupled to hyperbolic-meta material nano cavities. More details can be found in Ref 6.

References

1. X. Xu, W. Yao, D. Xiao, and T. F. Heinz, "Spin and pseudospins in layered transition metal dichalcogenides," Nat. Phys. *10*, 343–350 (2014).
2. K. F. Mak and J. Shan, "Photonics and optoelectronics of 2d semiconductor transition metal dichalcogenides," Nat. Photonics *10*, 216 (2016).
3. C. Indukuri, R. K. Yadav, and J. Basu, "Broadband room temperature strong coupling between quantum dots and metamaterials," Nanoscale *9*, 11418–11423 (2017).
4. X. Yang, J. Yao, J. Rho, X. Yin, and X. Zhang, "Experimental realization of three-dimensional indefinite cavities at the nanoscale with anomalous scaling laws," Nat. Photonics *6*, 450 (2012).
5. S. R. K. C. Indukuri, J. Bar-David, N. Mazurski, and U. Levy, "Ultrasmall mode volume hyperbolic nanocavities for enhanced light–matter interaction at the nanoscale," ACS Nano *13*, 11770 (2019).

Publications

1. S. R. K. C. Indukuri, C. Frydendahl, J. Bar-David, N. Mazurski, and U. Levy, "WS2 Monolayers Coupled to Hyperbolic Metamaterial Nanoantennas: Broad Implications for Light–Matter-Interaction Applications," ACS Applied Nano Materials 3(10), 10226-10233 (2020).

V. Linking rotation and metamaterials – extended year report / B.Z. Steinberg and Nader Engheta

In this extended, 4-th year of the project, our effort was placed on the two parallel tracks that were already presented and discussed in our 2020 and 2021 reports. These are:

1. Quasi-static ED of rotating structures and metamaterials in their rest frame of reference
2. Rotating metamaterials, Gyroscopes, and century-old problems in number theory

Below we present the advances made in each of these tracks.

Quasi-static rest-frame ED of rotating structures and metamaterials

Many modern artificial electromagnetic materials are made of arrays of meta-atoms such as the omega-particle or the split-ring resonator (SRR) [1]. Their equivalent electrodynamics is nothing but that of LC circuits, shown schematically in Figure 1 below. The Quasi-static power series formalism for rest-frame low frequency ED presented in our 2020 report can be applied directly to these meta-atoms in order to study their internal dynamics as a function of the rotation rate Ω.

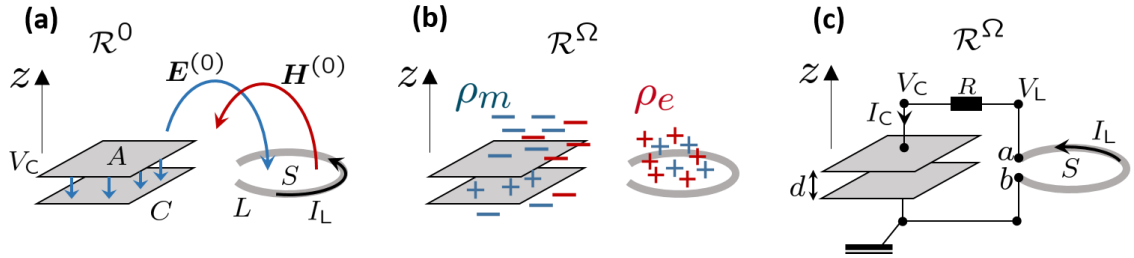

Figure 8. The ED in an equivalent LC circuit rest-frame rotating around the z-axis. (a) The zero-order fields E^0 (blue) and H^0 (red) are obtained from the stationary system solutions. (b) $\hat{z}\cdot E^0$ and $\hat{z}\cdot H^0$ generate rotation induced magnetic and electric charges $\rho_m = -2\Omega c^{-2}\,\hat{z}\cdot E^0$, and $\rho_e = 2\Omega c^{-2}\,\hat{z}\cdot H^0$. (c) the combined LC circuit with rotation induced gain mechanism due to the fictitious charges, as given by Eq.(1) below.

The rotation induced fictitious electric and magnetic charge are the source of gain mechanism, cast in the most general form by an equation that is a generalization of Eq.3 in our 2020 report

$$\omega_{1,2} = -i\omega_0^2(\sigma\Omega F + \tau/2) \pm \omega_0\sqrt{1-\omega_0^2\tau(\sigma\Omega F + \tau/4)} \qquad (1)$$

where $\sigma = \pm 1$ is the connection polarity (+1 for the connection shown in Fig.1), $F = [F_h(r_c)A + F_e(r_L)S]c^{-2}$, and where A, S are the capacitor and inductor effective areas, r_c, r_L are their centers, and

$$F_{e,h}(r) = \int \partial_z G(r,r')\ \hat{z}\cdot f_{e,h}(r')dv', \qquad G(r,r') \equiv [4\pi|r-r'|]^{-1} \qquad (2)$$

are in fact the fields due to the rotation induced fictitious charges. In the above, $f_{e,h}$ are the appropriately normalized radiation patterns of the devices zero-order (non-rotating) solutions

$$V_c\, f_e(r) = E^0(r), \qquad I_L f_h(r) = H^0(r) \qquad (3)$$

The result above, that applies for $e^{-i\omega t}$ time-dependence, shows that rotation-induced gain can exist not only in the artificial engineered core-shell particle discussed in our 2020 report. The gain or loss mechanism depends on the rotation direction (sign of Ω and on the connection polarity. Since many of the metamaterial design concepts are based on arrays of meta-atoms with essentially the same equivalent circuit, this new result potentially paves the way to a new type of metamaterials designed for energy harvesting applications and new rotation sensors.

The concept of rotation induced fictitious charge that exists even in a simple capacitor, suggests a new type of metamaterial functionalities. For example, the simple system shown in Fig. 2 is nothing but a realization of ***memristors*** [2,3], with memritance $M \equiv q/V = \Omega d/(c^2\epsilon)$. Interestingly, it can be positive or negative, depending on the rotation direction. Note also that ENZ materials can be used to increase M. Furthermore, unlike traditional implementation of memristors that are active and non-linear [3], this device is passive and linear. The use of memristor meta-atoms as the metamaterial building block will open the way to a whole new family of metamaterials.

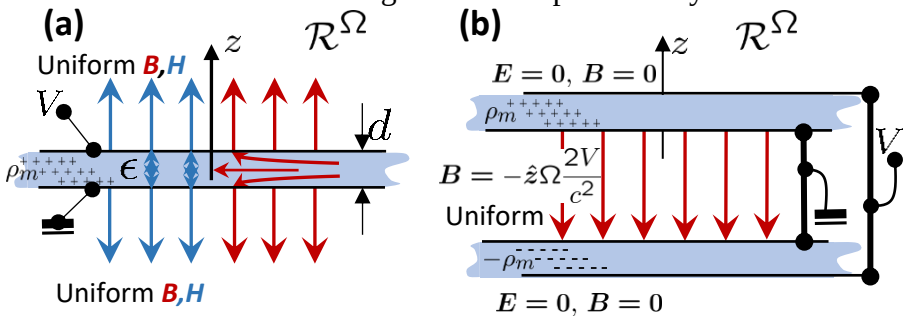

Figure 9. The rotation induced magnetic capacitor and the memristor. (a) A parallel plate electric capacitor filled with ϵ material possesses rotation induced fictitious magnetic charge $\rho_m = 2\Omega V/(dc^2)$ between its metal plates. This creates $B = \pm\hat{z}\,\Omega V c^{-2}$ @ $|z| > d/2$. (b) Two capacitors situated and connected as shown produce null B outside the structure, and uniform B inside the structure. This B is proportional to the voltage V and the rotation rate Ω, thus a memristor is created.

These results are derived and discussed in [4], among other new meta-atom functionalities.

Rotating metamaterials, Gyroscopes, and century-old problems in number theory

In our 2021 report we have demonstrated that a new type of metamaterials consisting of dielectric cylinder scatterers may exhibit a microscopic response that is rotation-sensitive. A surprising connection to the old "no three in line" problem, and the Heilbron triangle problem [5-8] was established. Furthermore, we have shown that arrays based on Erdős solution to the no three in line problem may exhibit sensitivity that significantly outperforms the rotation sensitivity of the classical Sagnac loop of equal area – see the 2021 report. However, while these solutions were the best we could find using a systematic, deterministic construction of the metamaterial array, one may ask whether this is the optimal (best-sensitivity) construction. The answer is No. In random array constructions, we may find rare realizations that outperform even the best performances of arrays based on the Erdős solutions. We have generated a database of 20K random arrays of 1450 scattaerers each, and simulated their EM response to rotation. We found that for some realizations can achieve a 5-fold better sensitivity. Our aim is to study their hidden-structure and explore their underlying physics by using ML methods. This idea is currently under investigation.

[1] S. Tretyakov, *Analytic Modeling in Applied Electromagnetics*. (Artech House, Boston), (2003).
[2] L.O. Chua, "Memristor – the missing circuit element," *IEEE Trans on Circuit Theory*, CT-**18**, 507-519 (1971).
[3] D.B. Strukov, G.S. Snider, D.R. Stewart, and R.S. Williams, "The missing memristor found," *Nature* **453**, 556 80–83 (2008).
[4] B.Z. Steinberg and N. Engheta, "Rest-frame quasi-static theory for rotating electromagnetic systems and circuits," to be submitted shortly.
[5] H. E. Dudeney, "A puzzle with pawns," *Amusements in Mathematics*, Nelson, Edinburgh, 1917.
[6] R. R. Hall, T. H. Jackson, A. Sudbery, and K. Wild, "Some advances in the No-Three-in-Line problem," *J. of Combinatorial Theory (A)* vol. 18, pp. 336-341, 1975.
[7] R. K. Guy, *Unsolved problems in number theory*, Problem books in mathematics, 3rd Ed., Springer 2004.
[8] K. F. Roth, "On a problem of Heilbronn," *J. of the London Math Soc.*, vol. 26(3), pp. 198-2014, 1951

VI. Cavity-less unidirectional laser / P. Sebbah

(Collaboration with A. A. Chabanov, UTSA, and I. Vitebskiy, AFRL)

Although the constitutive components of a photonic crystal are perfectly transparent, their periodic arrangement may block electromagnetic wave transmission at certain frequencies, when the wavelength becomes comparable to the spatial period [1]. Spatial periodicity results in strong anomalous dispersion and band gap structures similar to that of electrons in semiconductors and metals. Most of the photonic crystal materials respect spectral reciprocity and have a dispersion relation $\omega(\vec{k})$ which is symmetric with respect to $\vec{k}$. Only specific periodic arrangements can produce spectral asymmetry and non-reciprocal dispersion relation, $\omega(-\vec{k}) \neq \omega(\vec{k})$.

In this project, we introduce a periodic structure with broken space inversion and time reversal symmetry [2]. We study the problem of a microwave incident on the surface of a periodic structure with unit cell including two anisotropic dielectric layers and a magnetic layer (Fig. 12). This magnetic photonic crystal has a dispersion relation which supports a stationary inflection point (SIP) at which the group velocity vanishes (first and second derivative of $\omega(\vec{k})$ and a non-vanishing third derivative), giving rise to a peculiar resonance, called the "frozen mode" [3-6].

Low-loss magnetic materials with significant circular magnetic birefringence, as well as dielectric materials with high optical anisotropy are difficult to find in the optical regime. They are however readily available for microwaves. This is the regime we wish to explore in this project.

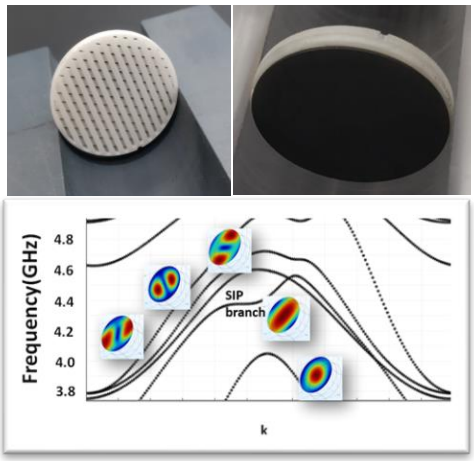

Figure 10: (Top) The unit cell of the MPC, including a magnetic layer (back) and two anisotropic dielectric layers, misoriented at an angle of 45°. Outer dimensions, 1". (Bottom) Stationary inflection point and non-symmetric dispersion relation of the MPC in full-3D simulation. Different branches corresponding to different transverse modes are represented.

The frozen mode is different in nature from edge modes near bandgaps because it does not result from the interference of 2 counter-propagating Bloch waves. It rather results from the interference of a slowly propagating wave and an evanescent wave. For this reason, the frozen mode is less sensitive to structural imperfection, boundary conditions and losses. Near this resonance, the transmittance of an incident wave is almost unity and unidirectional, as a consequence of non-reciprocity. Once it enters the slab, the wave slows down dramatically and its amplitude increases enormously, creating unique conditions for wave-matter interaction. We expect that in the presence of gain, the SIP will be naturally selected. These are the conditions we wish to bring together to design and test experimentally a cavity-less unidirectional maser [2].

Progress

In the last period of the project, we focused on the experimental setup, the characterization of the samples and the measurements of the structure. In June 2020, we received the first batch of anisotropic dielectric layers 3D-printed in the US, together with high quality rectangular horn antennas, used to control the polarization at emission and reception. Before the second lockdown due to the pandemic, we developed data processing routines to analyse the measurements of microwave transmission and we measured the frequency dependence of the electromagnetic characteristics of each component. After the second lockdown, we finalized the experimental setup

by including the electromagnet, which provides for magnetization saturation. We achieved to demonstrate non-symmetric dispersion in the presence of a saturating magnetic field.
In parallel to experiments, we explored numerically the dependence of the SIP frequency with different parameters, our objective being to be able to correct one parameter by another, so that a mismatched characteristic of the sample could be experimentally corrected. Second, we performed full-3D simulations to evaluate the difference between 2D and 3D modelling and to account for the transverse modes of the waveguide. We investigated the scaling of the SIP mode frequency with sample length and found a power law dependence.
Two papers are in preparation and a new collaboration has been established with Prof. Tsampikos Kottos at Wesleyan University.

Experiments

The experimental setup has been finalized. The polarized microwave field emitted and detected by the horn antenna is guided into and out of the sample via 0.5" Teflon rods. A vector network analyzer measures the reflected and transmitted fields vs. frequency in both directions (S-parameters: S_{11},S_{21},S_{22},S_{12}), amplitude and phase. Horn antennas can be 90°-rotated to change their respective polarization. This yields a full 2-ports 8x8 matrix, which fully characterizes the sample response to electromagnetic excitation. The sample is put between the 2 coils of a water-cooled electromagnet, yielding up to 0.3 T uniform magnetic field along the sample, to saturate the magnetization of the Ferrite layers. We developed an original de-embedding method, which removes the contribution due to elements other than the sample itself.

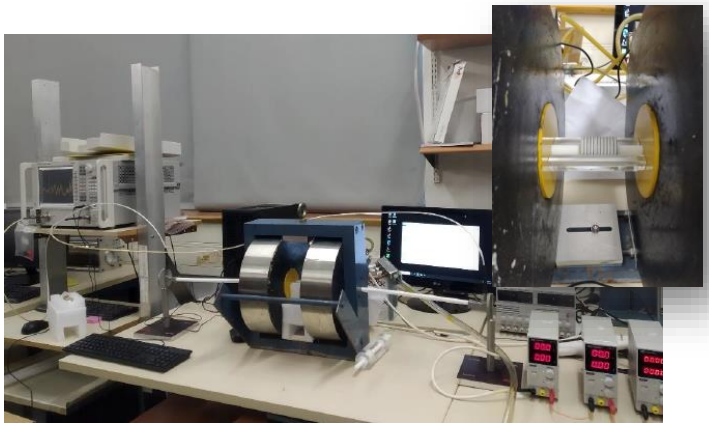

Figure 11: Experimental setup (see description in the text)

During the summer 2020, we measured the tensor of dielectric permittivity of the zirconia anisotropic layers. From the measure of the group delay, $d\phi/d\omega$, and after time gating, we obtained the frequency dependence of $\epsilon_\perp$and $\epsilon_\parallel$. Reasonable agreement is found, which validates the geometry and the fabrication chosen. Small discrepancy at working frequencies may however affects the prediction of the frozen mode. Our strategy is to correct it by changing another parameter in the experiment. This has been explored numerically (see numerical simulations).

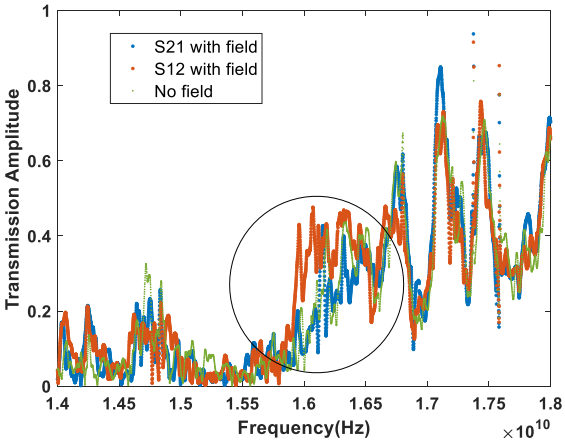

Figure 12: Comparison of S_{21} (blue) and S_{12} (red) with magnetic field applied. Without magnetic field, S_{21}=S_{12} (green). Note the gap below 16GHz and the region above the gap (circle) with strong asymmetry. The frozen mode is expected to appear in this region.

In spring 2021, we measured the transmission of the MPC, with up to 20 units, in absence and presence of a magnetic field to saturate magnetization (Fig. 14). We studied the position of the photonic bandgap as a function of the angle difference $\phi_2 - \phi_1$ between the two anisotropic dielectric layers. We showed that a frequency window exists where S21 and S12 are significantly different in the presence of the

magnetic field, which demonstrates the Faraday effect in a spectral region of strong asymmetry of the dispersion curve. The frozen mode is expected to appear in this region, but has not been identified yet.

Numerical simulations

We consider a unit cell composed of 2 anisotropic dielectric layers and one magnetic layer. Anisotropic layers are made of parallel bars in the experiment. In the simulations, they are replaced by homogeneous anisotropy for simplification. Full-3D FEM computations are performed to compute the band diagram, using COMSOL Multiphysics. We work at low frequency (4 GHz) compare to experiments (10 GHz), to reduce computation time and decrease the number of transverse modes.

A system exhibiting a SIP for a particular dispersion relation is found by an optimization algorithm to find the corresponding physical parameters (angle between anisotropic dielectric layers at given amplitude of magnetic field). The frequency at which the SIP occurs (infinite system) is found with 1 Hz precision to be SIP@4.376330259 GHz. The corresponding transverse profile is identified and will serve to "recognize" this mode (Fig. 10).

In a finite-length sample, longitudinal modes are discretized spectrally. It is therefore unlikely that a longitudinal mode be found at the exact SIP frequency. Besides, the resonant frequency acquires now an imaginary part due to the leakage on the two ends of the sample. As sample length L increases, the imaginary part of the mode ω_L closest spectrally to the SIP vanishes (Fig. 11a) as well as its spectral distance to the SIP frequency, $\omega_L - \omega_{SIP}$. This distance is found to scale as $(\omega_L - \omega_{SIP}) \sim L^{-1.17}$ (Fig. 11b). This result is confirmed and explained theoretically by the group of T. Kottos. For L=100-unit cells, the mode closest to the SIP frequency is identified by its frequency and its transverse profile (similar to profile in Fig. 10). In contrast to FP modes, the spatial distribution of the SIP mode is clearly non-symmetric (Fig. 12).

We have computed the scattering parameters which is the measure accessible to the experiment. We consider a sample with 20 layers, in a 2 port-geometry, with two possible transverse linear polarizations, x and y, for both the input and output fields. This can be described by a 4x4 scattering matrix:

$$S = \begin{pmatrix} S_{11}^{xx} & S_{11}^{xy} & S_{12}^{xx} & S_{12}^{xy} \\ S_{11}^{yx} & S_{11}^{yy} & S_{12}^{yx} & S_{12}^{yy} \\ S_{21}^{xx} & S_{21}^{xy} & S_{22}^{xx} & S_{22}^{xy} \\ S_{21}^{yx} & S_{21}^{yy} & S_{22}^{yx} & S_{22}^{yy} \end{pmatrix}.$$

If S is not symmetric, $S \neq S^T$, reciprocity is broken. Here we compare S_{21}^{xx} and S_{12}^{xx} with and without magnetic field. A difference between these 2 parameters is enough to demonstrate non-reciprocity. Without magnetic field, both S_{21}^{xx} and S_{12}^{xx} are identical. In the presence of a magnetic field, $S_{21}^{xx} \neq S_{12}^{xx}$ and reciprocity is broken. Non-reciprocity is maximized at 4.3763 GHz, close to SIP frequency, with a dip in S_{12}^{xx} and a peak in S_{21}^{xx}. This is in contrast with FP modes (e.g. at 4.33 GHz) where a maximum is found for both coefficients. The reason for it is that a FP resonance is a standing wave resulting from the interference of contra-propagating waves, $+k$ and $-k$, with same group velocity. So, reciprocity is maintained. A frozen mode in contrast is a resonance for one direction of propagation $k_1(\omega_{SIP})$ (slow mode). Because of the asymmetry, the opposite component, $-k_2(\omega_{SIP})$, corresponds to a rapid traveling wave (no

inflection point on this side of the dispersion relation). So, transmission (S_{21}^{xx}) in k_1 direction is enhanced (resonance), while it is small (S_{12}^{xx}) in the opposite direction $-k_2$.
We propose to characterize the frozen mode by its response to varying dissipation loss in the material. This is achieved by introducing an imaginary part in the dielectric material. Interestingly, for the SIP mode, S_{21}^{xx} increases with decreasing absorption, while S_{12}^{xx} remains small (Fig. 5a-c). The k_1 component is sensitive to the loss, while the fast component $-k_2$ is weakly affected. This is in contrast with FP resonances where both S-parameters increase with decreasing absorption.
To improve readability of the data, we use a metallic pinhole mask at input and output to reduce the number of transverse modes and reduce modal overlap.
Finally, A layered MPC structure exhibiting wave dispersion with a stationary inflection point (SIP) has been proposed. From numerical simulations, physical parameters have been optimized to induce a non-symmetrical band diagram and exhibit a SIP branch. In the finite-length sample, a frozen mode (closest longitudinal mode to the SIP frequency) has been identified and its intensity profile was found to be asymmetric, in contrast to FP modes which remain symmetric, even in the presence of a magnetic field. We propose to discriminate between frozen modes and FP modes, by varying dissipation loss. This signature is used to demonstrate the existence of a frozen mode in MPC in the microwave regime. Interestingly, the method we used to undo absorption and identify the frozen mode gives also indication about the effect of gain on the frozen mode. Introducing gain enhances the frozen mode faster than FP modes. Laser oscillations are therefore most likely to start at the SIP frequency. This is a first step in the demonstration of unidirectional "masing" action. A possible route to implement gain in the microwave regime is to introduce gain via NV-centers [9]. We believe our MPC geometry is unique to implement gain and to demonstrate unidirectional Maser based on gain selection of a frozen mode.

References

[1] J. Joannopoulos, R. Meade, and J. Winn, *Photonic crystals – molding the flow of light*, (Princeton University Press, Princeton, 1995).
[2] H. Ramezani, S. Kalish, I. Vitebskiy, and T. Kottos, Unidirectional lasing emerging from frozen light in nonreciprocal cavities, *Phys. Rev. Lett.* 112, 043904 (2014).
[3] A. Figotin and I. Vitebskiy, Electromagnetic unidirectionality in magnetic photonic crystals, *Phys. Rev.* B 67, 165210 (2003).
[4] A Figotin and I. Vitebskiy, Oblique frozen modes in periodic layered media, Phys. Rev. E 68, 036609 (2003).
[5] A. Figotin and I. Vitebskiy, Nonreciprocal magnetic photonic crystals, *Phys. Rev. E* 63, 066609 (2001).
[6] A. Figotin and I. Vitebskiy, Slow wave phenomena in photonic crystals, *Laser Photonics Rev*. 5, No. 2, 201–213 (2011)
[7] N. Apaydin, L. Zhang, K. Sertel, and J. L. Volakis, Experimental Validation of Frozen Modes Guided on Printed Coupled Transmission Lines, IEEE Trans. Microwave Theory&Techniques, 60, pp. 1513 - 1519 (2012).
[8] R. A. Chilton and R. Lee, Frozen Modes in Parallel-Plate Waveguides Loaded With Magnetic Photonic Crystals, *IEEE Trans.Micro.Theo.Tech.* 55, 2631 (2007).
[9] L. Jin, M. Pfender, N. Aslam, P. Neumann, S. Yang, J. Wrachtrup & R-B Liu, Proposal for a room-temperature diamond maser, *Nature Comm.* 6, 8251 (2015).